Detecting Covariance Symmetries in Polarimetric SAR Images

L. Pallotta, *Member, IEEE*, C. Clemente, *Member, IEEE*, A. De Maio, *Fellow, IEEE*, and J. J. Soraghan, *Senior Member, IEEE.*

***Abstract*— The availability of multiple images of the same scene acquired with the same radar but with different polarizations, both in transmission and reception, has the potential to enhance the classification, detection and/or recognition capabilities of a remote sensing system. A way to take advantage of the full-polarimetric data is to extract, for each pixel of the considered scene, the polarimetric covariance matrix, coherence matrix, Muller matrix, and to exploit them in order to achieve a specific objective.**

A framework for detecting covariance symmetries within polarimetric SAR images is here proposed. The considered algorithm is based on the exploitation of special structures assumed by the polarimetric coherence matrix under symmetrical properties of the returns associated with the pixels under test. The performance analysis of the technique is evaluated on both simulated and real L-band SAR data, showing a good classification level of the different areas within the image.

***Index Terms*— Polarimetric SAR image, radar image classification, coherence and covariance scattering matrix.**

I. Introduction

Polarimetric SAR imaging and the information obtainable from this kind of sensor configuration are attracting great interest from the research and end-user communities in recent years. Benefits, provided by the availability of multiple images of the same scene acquired with the same radar but with different polarizations, both in transmission and reception (HH, HV, and VV), include enhancing the classification, detection and/or recognition capabilities of the entire system. Among the different techniques available in open literature [1], a possible approach is to take advantage of the full-polarimetric data extracting for each pixel of the considered scene the polarimetric covariance matrix, coherence matrix, Muller matrix and so on, [1], [2], [3], [4], and to use them in order to achieve a specific objective. Usually, the quantity measured by a polarimetric radar is the well known scattering matrix [3] (also called Sinclair matrix [1, pag. 63]); however, it is very useful to express the latter in a vectorized form and compute some second order moment-based metrics, i.e. covariance and coherence matrices, that can be utilized to have inference about the scattering mechanisms characterizing the objects in the scene of interest. Moreover, a widely accepted processing strategy to deal with polarimetric SAR images relies on the coherent decomposition of the polarimetric scattering matrix. In this context, the Pauli [5], Krogager [6], and Cameron [7] decompositions play a central role. The aim of all these decompositions is to represent the scattering matrix as a combination of the scattering responses of independent elements (for instance single/odd-bounce scattering and double/even-bounce scattering), to associate a physical mechanism with each component and to extract relevant characteristics from polarimetric data sets.

An example of application of polarimetry can be found in [8], where the coherence matrix is exploited for extracting average parameters from experimental data. The algorithm is based on a second order statistical model which does not require any specification of the underlying multivariate statistical distribution. In fact it makes the assumption that in each cell there is always a dominant average scattering mechanism and, then, the parameters of this average component are estimated and related to the physical structures of the observed objects. Another example can be found in [9], where the use of both amplitude and phase information of the HH, HV, and VV images is introduced to distinguish among different scattering behaviours. By doing so, it is possible to interpret radar images and, in addition, to provide information aiding surface characterization through modelling of the polarimetric response of different types of terrain. In [10], the authors propose a new model for vegetation scattering mechanisms of mountainous forests, extending the classic radiative transfer model and taking into account the sloping ground surface under vegetation canopy. Finally, many other works in the last few years use polarimetry: for oil spills detection [11], [12], for ice thickness retrieval [13], and for feature detection within a SAR image [14].

In this paper, we propose and analyse a framework for detecting covariance symmetries within a polarimetric SAR image, through the exploitation of special structures assumed by the covariance (and consequently by the coherence) matrix under symmetrical properties of the returns associated to the pixels under analysis. Since our problem is formulated in terms of a composite hypothesis test including nested instances, the classic Generalized Maximum Likelihood (GML) approach [15] does not prove useful. In fact, it always leads to the selection of the hypothesis with the higher degree of uncertainty and which incorporates the nested instances [15], [16]. In order to circumvent this drawback, it is paramount

L. Pallotta is with Centro Regionale Information Communication Technology (CeRICT) scrl, via Cinthia c/o Complesso Universitario di Monte Sant'Angelo, Fabbr. 8B - 80126 Napoli, Italy. E-mail: luca.pallotta@unina.it.

C. Clemente and J. J. Soraghan are with University of Strathclyde, Centre for Excellence in Signal and Image Processing, EEE, 204, George Street, G1 1XW, Glasgow, UK. E-mail: carmine.clemente@strath.ac.uk, j.soraghan@strath.ac.uk.

A. De Maio is with Università degli Studi di Napoli "Federico II", Dipartimento di Ingegneria Elettrica e delle Tecnologie dell'Informazione, Via Claudio 21, I-80125 Napoli, Italy. E-mail: ademaio@unina.it.

to consider a modified version of the GML to accommodate nested signal models. Specifically, it is necessary to add to the GML (under each hypothesis) a penalty term related to the number of parameters to estimate; this leads to the so-called model order selection techniques [17], [18], [19] [20] to classify each pixel on the base of the corresponding coherence matrix structure. The knowledge of the symmetry would then allow enhanced performance for applications like knowledge-based GMTI (Ground Moving Target Indicator), oil spill detection and land cover classification.

The remainder of the paper is organized as follows. In Section II, the problem is introduced, while in Section III the proposed framework for detecting covariance symmetries is developed. The performance of the proposed technique applied on simulated and real L-band SAR data is presented and discussed in Section IV. Finally, in Section V, some concluding remarks are given.

NOTATION

We adopt the notation of using boldface for vectors $\boldsymbol{a}$ (lower case), and matrices $\boldsymbol{A}$ (upper case). The conjugate and conjugate transpose operators are denoted by the symbols $(\cdot)^*$ and $(\cdot)^\dagger$ respectively, whereas the symbol $(\cdot)^+$ denotes the pseudo-inverse. $\mathrm{tr}\{\cdot\}$ and $\det(\cdot)$ are respectively the trace and the determinant of the square matrix argument. $\boldsymbol{I}$ and $\boldsymbol{0}$ denote respectively the identity matrix and the matrix with zero entries (their size is determined from the context). $\mathbf{diag}(\boldsymbol{a})$ indicates the diagonal matrix whose i-th diagonal element is the i-th entry of $\boldsymbol{a}$. The letter j represents the imaginary unit (i.e. $j = \sqrt{-1}$). For any complex number x, $|x|$ represents the modulus of x, $\mathrm{Re}\{x\}$ is its real part, and $\mathrm{Im}\{x\}$ is its imaginary part. Moreover, $\mathcal{H}_n^{++}$ is the set of $n \times n$ positive semi-definite (psd) Hermitian matrices, $\mathcal{S}_n^{++}$ is the set of $n \times n$ psd symmetric matrices, and $\mathcal{P}_n^{++}$ is the set of $n \times n$ real psd persymmetric matrices[1]. Finally, $\mathbb{E}[\cdot]$ denotes statistical expectation.

II. PARAMETERS DEFINITION AND DATACUBE CONSTRUCTION

A multi-polarization SAR sensor, for each pixel of the image under test, measures $N = 3$ complex returns, which are collected from three different polarimetric channels (namely HH, HV, and VV). The N returns associated with the same pixel are organized in the specific order HH, HV, and VV to form the vector $\boldsymbol{X}(l, m)$, $l = 1, \dots, L$ and $m = 1, \dots, M$ (L and M represent the vertical and horizontal size of the image, respectively). Therefore, the sensor provides a 3-D data stack $\boldsymbol{X}$ of size $M \times L \times N$ which is referred to as datacube in the following, whose pictorial representation is given in Fig. 1.

Starting from the datacube $\boldsymbol{X}$ of the scene illuminated by the radar, for each pixel under test, we extract a rectangular neighbourhood $\mathcal{A}$ of size $K = W_1 \times W_2 \geq N$. We denote by $\boldsymbol{R}$ the matrix whose columns are the vectors of the polarimetric returns from the pixels of $\boldsymbol{X}$ which fall in the region $\mathcal{A}$. The matrix $\boldsymbol{R}$ is modelled as a random matrix, whose columns are assumed statistically independent and identically distributed random vectors drawn from a complex circular zero-mean Gaussian distribution with positive definite covariance matrix $\boldsymbol{C}$.

III. COVARIANCE SYMMETRIES DETECTION

The framework proposed in this paper uses the special structures assumed by the covariance and, consequently, by the corresponding coherence matrix over objects that scatter with a specific symmetry property [1, pp. 69-72], [2]. In this section we illustrate such structures arising when some important scattering symmetric properties become predominant, and then we introduce some algorithms that allow the detection of the specific covariance symmetry.

We consider the polarimetric covariance matrix in the presence of a reciprocal medium [1], [2] which is a 3×3 Hermitian matrix, i.e.

$$\boldsymbol{C} = \begin{bmatrix} c_{hhhh} & c_{hhhv} & c_{hhvv} \\ c_{hhhv}^* & c_{hvhv} & c_{hvvv} \\ c_{hhvv}^* & c_{hvvv}^* & c_{vvvv} \end{bmatrix}, \tag{1}$$

completely described by $n = 9$ real scalar values. In fact, the diagonal entries of this matrix are the conventional backscattering coefficients, which are real quantities, whereas the off-diagonal elements are complex values.

Let us consider, now, the presence of a reflection symmetry with respect to a vertical plane. It is usually observed over horizontal natural environments and produces complete decorrelations between the co-polarized and the cross-polarized elements (the details regarding the proof of this covariance structure can be found in [2]). Consequently, the covariance matrix under reflection symmetry assumes the following special form, which is fully described by $n = 5$ real scalar values, namely

$$\boldsymbol{C} = \begin{bmatrix} c_{hhhh} & 0 & c_{hhvv} \\ 0 & c_{hvhv} & 0 \\ c_{hhvv}^* & 0 & c_{vvvv} \end{bmatrix}. \tag{2}$$

From a physical point of view, this result is valid for volume scattering, surface scattering, or volume-surface interactions to all scattering orders, or to the total scattering effects no matter how dense is the medium, or how rough is the surface as long as the scattering configuration has the reflection symmetry [2].

Let us consider, now, the presence of a rotation symmetry, that is characterized by a covariance matrix invariant under the rotation around an axis by any considered angle [2]. Consequently, the polarimetric covariance matrix assumes the following special structure, completely described by $n = 3$

[1]A real persymmetric matrix $\boldsymbol{C}_n$ is a matrix with the following property $\boldsymbol{C}_n = \boldsymbol{J}\boldsymbol{C}_n^T\boldsymbol{J}$, with $\boldsymbol{J}$ the $n \times n$ permutation matrix

$$\boldsymbol{J} = \begin{bmatrix} 0 & 0 & \cdots & 0 & 0 & 1 \\ 0 & 0 & \cdots & 0 & 1 & 0 \\ 0 & 0 & \cdots & 1 & 0 & 0 \\ \vdots & \vdots & & \vdots & \vdots & \vdots \\ 0 & 1 & \cdots & 0 & 0 & 0 \\ 1 & 0 & \cdots & 0 & 0 & 0 \end{bmatrix}.$$

real scalar values, i.e.

$$\boldsymbol{C} = \begin{bmatrix} c_{hhhh} & c_{hhhv} & c_{hhvv} \\ -c_{hhhv} & c_{hvhv} & c_{hhhv} \\ c_{hhvv} & -c_{hhhv} & c_{hhhh} \end{bmatrix}, \tag{3}$$

where c_{hhhv} is purely imaginary, c_{hhvv} is purely real, and $c_{hvhv} = (c_{hhhh} - c_{hhvv})/2$. For instance, a chiral medium made by embedding helixes in an isotropic background can be considered as having both reciprocity and rotation symmetry [2].

Finally, the azimuth symmetry arises as the combination of a rotation symmetry with a reflection symmetry in any plane which contains the rotation symmetry axis. It can be observed for dense volumetric environments [3] and the corresponding polarimetric covariance matrix shares the form

$$\boldsymbol{C} = \begin{bmatrix} c_{hhhh} & 0 & c_{hhvv} \\ 0 & c_{hvhv} & 0 \\ c_{hhvv} & 0 & c_{hhhh} \end{bmatrix}, \tag{4}$$

where $c_{hvhv} = (c_{hhhh} - c_{hhvv})/2$. Evidently (4) is entirely described by $n = 2$ real scalar values.

With the above models for the polarimetric covariance matrix structure, we focus on the problem of data classification exploiting the scattering properties of the pixel under test and of a set of neighborhood pixels. Specifically, we associate to each pixel an "average" or "dominant" symmetry property on the base of the specific structure assumed by its covariance matrix. Moreover, to simplify the analytic tractability, we move to a transformed matrix domain (as described in Lemma 3.1) where some redundant information (contained in the functionally dependent coefficients of the covariance) translate into zeros of the corresponding transformed matrix. Before proceeding further, it is necessary to define the multiple hypotheses associated to the problem under consideration, i.e.

$$\begin{cases} H_1: & \text{no symmetry;} \\ H_2: & \text{reflection symmetry;} \\ H_3: & \text{rotation symmetry;} \\ H_4: & \text{azimuth symmetry.} \end{cases} \tag{5}$$

Hence, in Lemma 3.1 we show how to compute the transformed matrix from the covariance and determine its structure under the hypotheses $H_1, \dots, H_4$.

Lemma 3.1: Let us denote by

$$\boldsymbol{U} = \begin{bmatrix} 1 & 0 & 0 \\ 0 & 0 & 1 \\ 0 & 1 & 0 \end{bmatrix},$$

$$\boldsymbol{E} = \begin{bmatrix} 1 & 0 & 0 \\ 0 & 1/\sqrt{2} & 0 \\ 0 & 0 & 1 \end{bmatrix},$$

$$\boldsymbol{T} = \frac{1}{\sqrt{2}} \begin{bmatrix} 1 & 0 & 1 \\ 1 & 0 & -1 \\ 0 & \sqrt{2} & 0 \end{bmatrix},$$

$$\boldsymbol{V} = \begin{bmatrix} 1 & 0 & 0 \\ 0 & 0 & j \\ 0 & 1 & 0 \end{bmatrix},$$

four transformation matrices, where $\boldsymbol{U}$ is orthogonal, whereas $\boldsymbol{V}$ and $\boldsymbol{T}$ are unitary.

Then, under the reflection symmetry hypothesis

$$\boldsymbol{U}\boldsymbol{C}\boldsymbol{U}^\dagger = \begin{bmatrix} c_{hhhh} & c_{hhvv} & 0 \\ c^*_{hhvv} & c_{vvvv} & 0 \\ 0 & 0 & c_{hvhv} \end{bmatrix} = \begin{bmatrix} \boldsymbol{C}_1 & \boldsymbol{0} \\ \boldsymbol{0} & c \end{bmatrix}, \tag{6}$$

where $\boldsymbol{C}_1 \in \mathcal{H}_2^{++}$ and c is a positive real number.

Under the rotation symmetry hypothesis

$$\begin{aligned} &\boldsymbol{V}\boldsymbol{E}\boldsymbol{T}\boldsymbol{C}\boldsymbol{T}^\dagger\boldsymbol{E}\boldsymbol{V}^\dagger = \\ &\begin{bmatrix} c_{hhhh} + c_{hhvv} & 0 & 0 \\ 0 & c_{hvhv} & \mathrm{Im}\{c_{hhhv}\} \\ 0 & \mathrm{Im}\{c_{hhhv}\} & c_{hvhv} \end{bmatrix} \\ &= \begin{bmatrix} a & \boldsymbol{0} \\ \boldsymbol{0} & \boldsymbol{C}_2 \end{bmatrix}, \end{aligned} \tag{7}$$

where $\boldsymbol{C}_2 \in \mathcal{P}_2^{++}$, and a is a positive real number.

Finally, under the azimuth symmetry hypothesis

$$\begin{aligned} \boldsymbol{E}\boldsymbol{T}\boldsymbol{C}\boldsymbol{T}^\dagger\boldsymbol{E} &= \begin{bmatrix} c_{hhhh} + c_{hhvv} & 0 & 0 \\ 0 & c_{hvhv} & 0 \\ 0 & 0 & c_{hvhv} \end{bmatrix} \\ &= \begin{bmatrix} a & 0 & 0 \\ 0 & b & 0 \\ 0 & 0 & b \end{bmatrix}, \end{aligned} \tag{8}$$

where b is a positive real number.

Proof: The proof is omitted since it can be obtained performing the matrix multiplications at the right hand side of (6)-(8). ■

Let us consider the complex multivariate probability density function (pdf) of the observable matrix $\boldsymbol{R}$, i.e.

$$f_{\boldsymbol{R}}(\boldsymbol{R}|\boldsymbol{C}) = \frac{1}{\pi^{3K}\left[\det(\boldsymbol{C})\right]^K} \exp\left\{-\mathrm{tr}\left(\boldsymbol{C}^{-1}\boldsymbol{R}\boldsymbol{R}^\dagger\right)\right\}, \tag{9}$$

the Fisher-Neyman factorization theorem [15] implies that $\boldsymbol{S}_0 = \boldsymbol{R}\boldsymbol{R}^\dagger$ is a sufficient statistic for $\boldsymbol{C}$.

Now, the maximum likelihood estimate of $\boldsymbol{C}$ can be obtained as the optimal solution to the optimization problem

$$\begin{aligned} \max_{\boldsymbol{C}} \log\left(f_{\boldsymbol{R}}(\boldsymbol{R}|\boldsymbol{C})\right) = -K \min_{\boldsymbol{C}} &\left[\log\det(\boldsymbol{C})\right. \\ &\left.+\mathrm{tr}\left(\boldsymbol{C}^{-1}\boldsymbol{S}\right)\right] - 3K\log\pi, \end{aligned} \tag{10}$$

where $\boldsymbol{S} = \frac{1}{K}\boldsymbol{S}_0$.

The following proposition shows the form assumed by the optimal value of problem (10), as well as the ML optimizer, in the presence of the four different scattering symmetries previously described.

Proposition 3.2: The optimal value of

$$\min_{\boldsymbol{C}\in\mathcal{H}_3^{++}} \left[\log\det(\boldsymbol{C}) + \mathrm{tr}\left(\boldsymbol{C}^{-1}\boldsymbol{S}\right)\right] \tag{11}$$

and the corresponding optimal solution $\check{\boldsymbol{C}}$ are respectively given by:

1) No symmetry:

$$\log\det(\boldsymbol{S}) + 3.$$

$$\check{\boldsymbol{C}} = \boldsymbol{S}.$$

2) Reflection symmetry:

$$\log\det\left(\bar{\boldsymbol{S}}_{1,1}\right)+\log\left(\bar{S}_{3,3}\right)+3,$$

$$\breve{\boldsymbol{C}}=\boldsymbol{U}^{\dagger}\begin{bmatrix}\bar{\boldsymbol{S}}_{1,1} & \boldsymbol{0}\\ \boldsymbol{0} & \bar{S}_{3,3}\end{bmatrix}\boldsymbol{U},$$

where $\bar{\boldsymbol{S}}=\boldsymbol{U}\boldsymbol{S}\boldsymbol{U}^{\dagger}=\begin{bmatrix}\bar{\boldsymbol{S}}_{1,1} & \bar{\boldsymbol{S}}_{1,3}\\ \bar{\boldsymbol{S}}_{3,1} & \bar{S}_{3,3}\end{bmatrix}$.

3) Rotation symmetry:

$$\log\det\left(\frac{1}{2}\left(\tilde{\boldsymbol{S}}_{2,2}+\boldsymbol{J}\tilde{\boldsymbol{S}}_{2,2}\boldsymbol{J}\right)\right)+\log\left(\tilde{S}_{1,1}\right)+3+\log 2,$$

$$\breve{\boldsymbol{C}}=\boldsymbol{T}^{\dagger}\boldsymbol{E}^{-1}\boldsymbol{V}^{\dagger}\begin{bmatrix}\tilde{S}_{1,1} & \boldsymbol{0}\\ \boldsymbol{0} & \frac{1}{2}\left(\tilde{\boldsymbol{S}}_{2,2}+\boldsymbol{J}\tilde{\boldsymbol{S}}_{2,2}\boldsymbol{J}\right)\end{bmatrix}\boldsymbol{V}\boldsymbol{E}^{-1}\boldsymbol{T},$$

where $\tilde{\boldsymbol{S}}=\boldsymbol{V}\boldsymbol{E}\boldsymbol{T}\boldsymbol{S}\boldsymbol{T}^{\dagger}\boldsymbol{E}\boldsymbol{V}^{\dagger}=\begin{bmatrix}\tilde{S}_{1,1} & \tilde{\boldsymbol{S}}_{1,2}\\ \tilde{\boldsymbol{S}}_{2,1} & \tilde{\boldsymbol{S}}_{2,2}\end{bmatrix}$.

4) Azimuth symmetry:

$$\log\left(\hat{S}_{1,1}\right)+2\log\left(\frac{\hat{S}_{2,2}+\hat{S}_{3,3}}{2}\right)+3+\log 2,$$

$$\breve{\boldsymbol{C}}=\boldsymbol{T}^{\dagger}\boldsymbol{E}^{-1}\mathbf{diag}\left(\hat{S}_{1,1},\frac{\hat{S}_{2,2}+\hat{S}_{3,3}}{2},\frac{\hat{S}_{2,2}+\hat{S}_{3,3}}{2}\right)\boldsymbol{E}^{-1}\boldsymbol{T},$$

where $\hat{\boldsymbol{S}}=\boldsymbol{E}\boldsymbol{T}\boldsymbol{S}\boldsymbol{T}^{\dagger}\boldsymbol{E}$ and $\hat{S}_{1,1}$, $\hat{S}_{2,2}$, $\hat{S}_{3,3}$ are its diagonal entries.

Proof: See Appendix A. ■

A. Model Order Selection

As previously discussed, we are focused on a composite multiple hypotheses testing problem which includes both nested and non-nested instances. The GML approach does not appear useful for this study since the likelihood always assumes the highest value under the H_1 hypothesis. Hence, to overcome this problem, we need to consider modified versions of the GML to accommodate nested instances. Specifically a penalty function that is dependent on the number of unknown elements to estimate is added to the GML under each hypothesis. This leads to the so-called model order selectors[2] [17], [18], [19], [20], that allow us to estimate the correct structure (the model order) from the available observables ($\boldsymbol{R}$ in this case). Following the above guidelines, it is necessary to evaluate a decision statistic under each hypothesis, and then the order is chosen as the one which corresponds to the minimum among the four statistics. Before proceeding further it is worth underlying that model order selection approaches have been already used in SAR remote sensing applications. In this context we mention [21], [22], [23], [24] for interferometric SAR, [25] with reference to double-scatterers detection in SAR tomography.

The general order selection rules proposed in [17] and [18] can be expressed through the corresponding decision statistics in the following compact form

$$-2\log\left(f\left(\boldsymbol{R}|\breve{\boldsymbol{C}}^{(n)}\right)\right)+n\,\eta(n,K), \tag{12}$$

with $\breve{\boldsymbol{C}}^{(n)}$ the ML estimate of $\boldsymbol{C}$ comprising of n parameters. The term $n\,\eta(n,K)$ is called penalty coefficient and its role can be intuitively explained observing that the first term in (12) decreases with increasing n (for nested models), whereas the second term increases. As a consequence, $n\,\eta(n,K)$ in (12) penalizes overfitting [18]. Different selection strategies diversify due to the definition of this quantity. Specifically, for

- AIC (Akaike Information Criterion): $\eta(n,K)=2$;
- GIC (Generalized Information Criterion): $\eta(n,K)=\rho+1$, with ρ an integer number greater than or equal to 2;
- BIC (Bayesian Information Criterion): $\eta(n,K)=\log(K)$.

For the case at hand, substituting (10), obtained as described in *Proposition* 3.2, in (12), it is not difficult to obtain the following decision statistic under each hypothesis (notice that for simplicity the dependency of η from n and K is omitted in the following equations):

- H_1 :

$$2K\log\det\left(\boldsymbol{S}\right)+6K+6K\log(\pi)+9\eta;$$

- H_2 :

$$2K\log\det\left(\bar{\boldsymbol{S}}_{1,1}\right)+2K\log(\bar{S}_{3,3})+6K+6K\log(\pi)+5\eta;$$

- H_3 :

$$2K\log\det\left(\frac{1}{2}\left(\tilde{\boldsymbol{S}}_{2,2}+\boldsymbol{J}\tilde{\boldsymbol{S}}_{2,2}\boldsymbol{J}\right)\right)+2K\log\left(\tilde{S}_{1,1}\right)+6K+2K\log 2+6K\log(\pi)+3\eta;$$

- H_4 :

$$2K\log\left(\hat{S}_{1,1}\right)+4K\log\left(\frac{\hat{S}_{2,2}+\hat{S}_{3,3}}{2}\right)+6K+2K\log(2)+6K\log(\pi)+2\eta.$$

A remark is now necessary: for the BIC, there are two particular assumptions on the Fisher information matrix $\boldsymbol{F}$ of the estimation problem. They are referred to as regularity conditions and their validity is shown in Appendix B.

The last decision criterion considered herein is referred to as Exponentially Embedded Families (EEF) approach; its general theoretical formulation is laid down in [20], i.e.

$$\mathrm{EEF}(i)=\left\{l_{G_i}(\boldsymbol{R})-n(i)\left[\log\left(\frac{l_{G_i}(\boldsymbol{R})}{n(i)}\right)+1\right]\right\}u\left(\frac{l_{G_i}(\boldsymbol{R})}{n(i)}-1\right), \tag{13}$$

with

$$l_{G_i}(\boldsymbol{R})=2\log\left(\frac{f(\boldsymbol{R};\breve{\boldsymbol{C}}^{(n(i))})}{f(\boldsymbol{R};\boldsymbol{C}^{(0)})}\right),\quad i=1,\ldots 4, \tag{14}$$

$n(i)$ the number of unknown parameters under the i-th hy-

[2]We recommend to the interested reader reference [18] for a methodological framework toward the definition of some model order selectors (together with the corresponding penalty terms) based on the Kullback-Leibler (KL) information criterion and the Bayesian theory.

pothesis, and $u(\cdot)$ the Heaviside step function, i.e. $u(\cdot) = 1$ if its argument is greater than 0, otherwise it is 0. In order to proceed further, it is necessary to evaluate the functions $l_{G_i}(\cdot)$, $i = 1, \ldots, 4$, in correspondence of the four hypotheses previously defined, but before doing this, we need to introduce a dummy hypothesis, H_0, where there is no dependency on the unknown parameters. Specifically, let us define the covariance matrix under the H_0 hypothesis, $\boldsymbol{C}^{(0)}$ as the N-dimensional identity matrix, i.e. $\boldsymbol{C}^{(0)} = \boldsymbol{I}_N$. With this choice, the functions $l_{G_i}(\cdot)$, $i = 1, \ldots, 4$, become:

- H_1 :
$$l_{G_1}(\boldsymbol{R}) = -2K \log\det(\boldsymbol{S}) - 6K + 2\mathrm{tr}(\boldsymbol{S}_0);$$
- H_2 :
$$l_{G_2}(\boldsymbol{R}) = -2K \log\det\left(\bar{\boldsymbol{S}}_{1,1}\right) - 2K\log(\bar{S}_{3,3}) - 6K + 2\mathrm{tr}(\boldsymbol{S}_0);$$
- H_3 :
$$l_{G_3}(\boldsymbol{R}) = -2K \log\det\left(\frac{1}{2}\left(\tilde{\boldsymbol{S}}_{2,2} + \boldsymbol{J}\tilde{\boldsymbol{S}}_{2,2}\boldsymbol{J}\right)\right) - 2K\log\left(\tilde{S}_{1,1}\right) - 6K - 2K\log(2) + 2\mathrm{tr}(\boldsymbol{S}_0);$$
- H_4 :
$$l_{G_4}(\boldsymbol{R}) = -2K\log\left(\hat{S}_{1,1}\right) - 4K\log\left(\frac{\hat{S}_{2,2} + \hat{S}_{3,3}}{2}\right) - 6K - 2K\log(2) + 2\mathrm{tr}(\boldsymbol{S}_0).$$

Finally, for both the AIC, BIC, and GIC, we select the hypothesis which corresponds the to minimum decision statistic, whereas for the EEF the one that corresponds to the maximum, namely

$$\hat{h}_{\text{AIC}} = \arg\min_h \text{AIC}(h), \quad (15)$$

$$\hat{h}_{\text{BIC}} = \arg\min_h \text{BIC}(h), \quad (16)$$

$$\hat{h}_{\text{GIC}} = \arg\min_h \text{GIC}(h), \quad (17)$$

$$\hat{h}_{\text{EEF}} = \arg\max_h \text{EEF}(h), \quad (18)$$

where $h = 1, \ldots, 4$ is the index identifying the specific hypothesis. In other words, for each pixel under test, the selected structure is the one associated to $H = H_{\hat{h}}$. For the sake of completeness and to help the reader to grasp all the details on the proposed procedure, in Algorithm 1, we have explicitly reported all the basic steps required to classify each pixel of the image. It refers to the order selector EEF. However, it is possible to consider other cases too, just substituting the EEF with the AIC, the BIC or the GIC and computing the minimum in place of the maximum, i.e. (15)-(17) instead of (18).

Algorithm 1 Covariance Symmetries Detection

Input: $K = W \times W$, $\boldsymbol{R}$ (constructed as described in Section III-A).
Output: $H_{\hat{h}}$.
1: Compute the matrices $\boldsymbol{S}_0$, $\boldsymbol{S}$, $\bar{\boldsymbol{S}}$, $\tilde{\boldsymbol{S}}$, and $\hat{\boldsymbol{S}}$ as defined in Proposition 3.2.
2: Compute the quantities EEF(h), $h = 1, \ldots, 4$, as described in (13).
3: Choose the index $\hat{h}$ associated with the maximum EEF as given in (18).
4: Associate to the pixel under test the label $H_{\hat{h}}$.

IV. Results

In this section, the performance of the proposed rules for covariance symmetry detection is assessed. In particular, to evaluate the effectiveness of the different techniques, both simulated and real radar data are considered.

A. Analysis on Simulated Data

In this subsection the performance analysis on simulated data for the order selectors introduced in Section III-A is developed and discussed. In particular, the probability of correct classification is estimated (resorting to Monte Carlo simulations) as the ratio between the number of correct classifications and the total number of trials MC which is set to 10^4. For each simulation run K 3-dimensional zero-mean complex circular Gaussian vectors are simulated. Hence, they are colored in order to exhibit a covariance matrix structure characterizing a specific hypothesis of the testing problem. As to the theoretical covariance matrices defining the four scenarios (no symmetry, reflection, rotation, and azimuth symmetry) they are respectively given by

$$\boldsymbol{C}_1 = \begin{bmatrix} 1 & 0.2+0.3j & 0.5-0.3j \\ 0.2-0.3j & 0.25 & -0.2-0.2j \\ 0.5+0.3j & -0.2+0.2j & 0.8 \end{bmatrix}, \quad (19)$$

$$\boldsymbol{C}_2 = \begin{bmatrix} 1 & 0 & 0.5-0.3j \\ 0 & 0.25 & 0 \\ 0.5+0.3j & 0 & 0.4 \end{bmatrix}, \quad (20)$$

$$\boldsymbol{C}_3 = \begin{bmatrix} 1 & 0.3j & 0.2 \\ -0.3j & 0.4 & 0.3j \\ 0.2 & -0.3j & 1 \end{bmatrix}, \quad (21)$$

$$\boldsymbol{C}_4 = \begin{bmatrix} 1 & 0 & 0.5 \\ 0 & 0.25 & 0 \\ 0.5 & 0 & 1 \end{bmatrix}. \quad (22)$$

In Fig. 2, the probability of correct classification (expressed in percentage) is reported for each of the four analyzed models, considering $K = 25$ data vectors. The sub-plots refer, respectively, to the four considered covariance scenarios, and the performance measures are related to five order selectors, i.e. AIC, BIC, GIC with $\rho = 2$, GIC with $\rho = 3$, and EEF. The results show that the EEF, the GIC and the BIC approaches provide a better performance than that achievable using the AIC. It is also worth observing that for small values of K all the selectors exhibit a performance degradation due to the fact that the sample covariance matrix achieves good estimation performances only when K is sufficiently higher than N. This estimation error becomes more impactful in cases where symmetries lead to similar structures in the covariance matrix. This situation arises with reference to the azimuth symmetry which shares a structure quite close to the rotation symmetry.

To study in details the behaviour of the proposed algorithm in the presence of a better and better covariance estimate, in Fig. 3 we report, for each selector, the probability of correct classification as a function of the number of looks, K. Again, the data are simulated as in Fig. 2, i.e. zero-mean complex circular Gaussian vectors with covariance matrix given by $\boldsymbol{C}_1$, $\boldsymbol{C}_2$, $\boldsymbol{C}_3$, and $\boldsymbol{C}_4$, respectively. Besides, 10^4 Monte Carlo runs have been utilized.

From this analysis it is clear that the case of symmetry absence is almost always correctly detected, independently of the utilized selector. Moreover, the azimuth symmetry case is the most challenging situation, in fact only the GIC is able to ensure a probability of correct classification higher than 90% for small values of K. Finally, the curves show that the performances improve as K increases, due to the better estimation of the covariance matrix thanks to the greater number of available homogeneous data. This agrees with the intuition that the more the available information about the scene the better the algorithms performance.

To conclude the study on simulated data, and to demonstrate a certain degree of robustness for the proposed algorithm with respect to the design hypotheses, we consider a mismodeling analysis where the data deviate from the Gaussian behavior; specifically, we model each column of the matrix $\boldsymbol{R}$, say $\boldsymbol{r}_k$ $k = 1, \ldots, K$, as a Spherically Invariant Random Vector (SIRV) [26], [27], [28] which can be written in the form

$$\boldsymbol{r}_k = \sqrt{\tau_k}\boldsymbol{g}_k, \quad k = 1, \ldots, K,$$

where τ_k is a positive real random variable (usually known as texture) and $\boldsymbol{g}_k$ is an N-dimensional zero-mean complex circular Gaussian vector, whose covariance matrix is set according to the four considered symmetry hypotheses, i.e. $\boldsymbol{C}_1$, $\boldsymbol{C}_2$, $\boldsymbol{C}_3$, and $\boldsymbol{C}_4$ respectively. In the simulations, we assume that $\tau_1, \tau_2, \ldots, \tau_K$ are statistically independent. Besides, they follow the Gamma distribution

$$f(x) = \frac{1}{\Gamma(\nu)} \frac{1}{\mu^{\nu}} x^{\nu-1} e^{-x/\mu} u(x),$$

where $\Gamma(\cdot)$ is the Eulerian Gamma function, μ and $\nu > 0$ are the scale and shape parameters, respectively (we set $\mu = 1/\nu$ in order to have a Gamma distribution with unit mean). The adopted model for the textures implies that the amplitude pdfs of $\boldsymbol{r}_k, \ldots, \boldsymbol{r}_K$ are K-distributed. The analysis is conducted for different values of the shape parameter, i.e. $\nu = (1, 2, 5, 10)$, and the results are reported in Figs. 4, 5, 6, and 7.

The curves clearly show that the GIC-, the BIC-, and EEF-based detectors outperform the AIC. Moreover, the classification in the fourth hypothesis still remains a challenge as the structure of $\boldsymbol{C}_4$ is quite close to that of $\boldsymbol{C}_3$. Nevertheless, this mismodeling analysis has highlighted that even in the presence of data that do not comply with Gaussianity, the proposed algorithm shares some robustness and is able to grant satisfactory symmetry classification performances.

B. Analysis on Real UAV-SAR Data

In this subsection, the results on real SAR data are shown and discussed. In particular, an L-band coherent polarimetric dataset[3] acquired using UAVSAR [29] on Southern California Coast on the 20th of November 2014[4] is utilized. The latter contains a scene acquired with three polarizations (HH, HV, and VV) and whose polarimetric overlay is shown in Fig. 8.

For our analysis, the selected area of interest is a sub-image of 2000×2000 pixels (i.e., $L = M = 2000$) containing both terrain and sea data. For comparison purposes, the span [1, p. 61] of such image (expressed in dB) is reported in Fig. 9(a), whereas in Fig. 9(b) it is represented its H-A-α decomposition [8] in RGB colors.

In Fig. 10, the detected symmetries for the reference image are plotted, using the AIC, BIC, GIC (with $\rho = 3$), and EEF, respectively, with $K = 25$, i.e. a 5×5 sliding window is utilized. Specifically, for each pixel of the considered scene, a specific colour is indicated, which is associated to the specific hypothesis chosen by the test.

The results show that the AIC is not able to achieve appreciable results in terms of classification of terrain data with respect to the sea one. Moreover, the EEF turns out to be the best order selector on this dataset, because it is able to show the largest amount of details within the image.

Reflection symmetry (blue pixels) is predominant on the sea area in Fig. 10, while the terrain area is classified as H_1 or H_2, meaning that no symmetry (black pixels) or reflection symmetry is detected; finally, the area separating sea and terrain areas is mainly classified as azimuthal symmetry (green pixels).

C. Analysis on Real AIR-SAR Data

To give an additional evidence of the effectiveness of the proposed algorithm, in this subsection, a second real SAR dataset is analyzed and the results are discussed. In particular, an L-band coherent polarimetric dataset[5] acquired in the 1988 from the JPL using an AIRSAR on the San Francisco Bay [1], [8] is utilized. The image (900×1024 pixels) contains a mixed urban, vegetation and sea scene, whose span is reported in Fig. 11(a). To give further information about the considered area, in Fig. 11(b) the corresponding H-A-α decomposition is depicted in RGB colors.

In Fig. 12, the detected symmetries are plotted using the AIC, BIC, GIC (with $\rho = 3$), and EEF, respectively, with $K = 25$, i.e. a 5×5 sliding window. As before, for each pixel of the considered scene, a specific color corresponds to a specific symmetry class.

The results confirm those obtained with the UAVSAR data: the GIC, BIC and EEF outperform the AIC. In fact, the different areas are clearly distinguished exploiting the BIC, the GIC, and EEF, whereas for the AIC some ambiguities arise with reference to the classification of the sea.

[3]The data can be downloaded at *http://uavsar.jpl.nasa.gov*.

[4]The specific acquisition is SSurge_15305_14170_007_141120_L090_CX_01

[5]The data can be downloaded at *https://earth.esa.int/web/polsarpro/data-sources/sample-datasets.*

However, comparing the BIC, GIC, and EEF assignment results in Fig. 12 with the span image in Fig. 11, it can be observed that the sea is classified as showing reflection symmetries (blue color). Moreover, the vegetation areas are classified as azimuth symmetric (green color), and the urban scenes are associated to the absence of any symmetry (black pixels). This is probably due to the strong heterogeneity of the environment precluding the rising of a dominant scattering symmetry. As a final remark, the number of pixels classified with rotation symmetry is very small.

To provide a more quantitative analysis, in Table I, the percentage of pixels classified as sharing the same symmetry is given for each order selector. Considering the EEF, the table highlights that the rotation symmetry is almost never observed (only the 1% of the pixels). Otherwise stated, there is a prevalence of the other symmetry classes: the percentage of pixels classified as exhibiting a rotation symmetry is the 30% (the majority of the sea pixels), whereas 23% are azimuth symmetric pixels mostly belonging to the vegetation areas. The remaining pixels do not exhibit any symmetry and are mainly located in the urban areas and in a particular sea zone where, as illustrated in Fig. 11 (span), there are very strong returns.

TABLE I: Real L-band data (AIRSAR San Francisco Bay JPL). Number of pixels (in percentage over the total) sharing a specific symmetry.

	AIC	BIC	GIC	EEF
H_1	74%	77%	50%	46%
H_2	13%	12%	28%	30%
H_3	2%	2%	1%	1%
H_4	11%	9%	21%	23%

D. Quantitative Comparison Between H/α and Symmetric H/α Classification

The scope of this subsection is to provide a quantitative comparison between the classic H/α classification and the one exploiting our algorithm as pre-processing stage (the block diagram illustrating the latter approach is shown in Fig. 13). Specifically, the covariance matrix estimate utilized to perform the H/α decomposition is the one provided by the EEF selector in place of the classic sample covariance matrix.

The H/α classification provides as output 9 classes which are explicitly defined within [1], [8]. To have a quantitative comparison, we compute the confusion matrix between the two mentioned classifications assuming as "reference" class the one assigned to each pixel by the H/α algorithm, while the test outcome is the class assigned by the symmetrical H/α approach.

From the confusion matrix, reported in Table II, it appears that the main difference between the two classifiers is in the selection of class 5. Specifically 31.23% of the pixels which belonged to class 5 according to the H/α classifier are associated to the class 2 by the symmetric H/α rule. This is tantamount to classifying pixels as high entropy vegetation scattering instead of medium entropy vegetation scattering. From the visual point of view (see Figs. 14(a) and 14(b)), it appears that the symmetric H/α rule provides more delineated borders of the vegetated region corresponding to the green rectangle located in the mid of the left part of Fig. 14. Moreover, structures corresponding to buildings would result more visible in the image produced by the symmetric H/α classification (i.e. pixels classified as 1 which are representative of double-bounces mechanisms). As an example, the reader could refer to the zones labelled with the letters A and B within the images of Fig. 14, where, in the case of symmetric H/α classifier, the *de Young Museum* (label A) and the *Alhoa Avenue* (label B) are more visible with respect to classic H/α classifier. In fact, with the symmetric algorithm they are associated to class 1 pixels, which correspond to returns from buildings.

E. Application for Oil Spill Symmetry Characterization

To further assess the performance of the proposed algorithms and their capabilities to distinguish among different areas within a scene, we apply them to a zone of the *GOMoil_07601_10052_101_100622_L090_CX_02* SAR image which is composed of sea data containing also an oil spill. The image has been acquired on 22nd of June 2010, during the British Petroleum oil spill incident in the Gulf of Mexico (known also as the Deepwater Horizon Oil Spill). As in the previous analysis, this second image contains a scene acquired with all the polarizations and the corresponding polarimetric overlay is reported in Fig. 15. Again, the selected area of interest is a sub-image of 2000×2000 pixels, whose span is displayed in Fig. 16(a) and its H-A-α decomposition in RGB colors in Fig. 16(b). This choice is, of course, for testing our techniques as well as to provide some suggestions on possible applications of the algorithm in real operative contexts.

We represent in Fig. 17, the detected symmetries for the reference image, computed using, respectively, the AIC, BIC, GIC (with $\rho = 3$), and EEF, with $K = 25$.

The results show that both the AIC and the BIC achieve quite good results in terms of classification of sea data with respect to oil spills, since the sea pixels are classified as reflection symmetry (blue pixels) whereas the oil spill shows some azimuthal symmetry (green pixels) in the radar returns. However, both the GIC and EEF outperform the AIC and BIC, with a clear separation of the different regions within the area under test. It is also interesting to observe a small strip characterized by an azimuthal symmetry (green pixels) in correspondence of a small ship transition over the sea (see the ellipse in Fig. 17).

V. CONCLUSIONS

We have introduced and analysed a new framework for detecting covariance symmetries within polarimetric SAR images. The proposed algorithm is based on the exploitation of the special structures assumed by the polarimetric coherence matrix whenever symmetrical properties of the returns associated to the pixels under analysis occur. Specifically, the core of the technique is the utilization of model order selectors, capitalizing the coherence matrix structures, to classify each pixel of the considered scene.

TABLE II: Real L-band data (AIRSAR San Francisco Bay JPL). Confusion Matrix (expressed in percentage) between the classic H/α classification and the one exploiting our algorithm as pre-processing stage. The values in the table are expressed in percentage.

Time [s] \ Symmetric H/α	**1**	**2**	**3**	**4**	**5**	**6**	**7**	**8**	**9**
1	99.49	0.51	0	0	0	0	0	0	0
2	10.03	89.97	0	0	0	0	0	0	0
3	0	0	0	0	0	0	0	0	0
4	4.10	8.41	0	87.48	0.01	0	0	0	0
5	0	31.23	0	3.76	58.10	6.91	0	0	0
6	0	0	0	0	1.78	98.22	0	0	0
7	0	0	0	0.43	0.01	0	99.56	0	0
8	0	0	0	0	5.74	0	0	94.26	0
9	0	0	0	0	0.01	0.85	0	0	99.14

The analysis of the new technique has been conducted on both simulated and real SAR data. In particular, the former has shown good capabilities to correctly classify the data in a controlled environment. Moreover, the latter has demonstrated the effectiveness of the approach and its flexibility to be integrated in operative context and algorithms, such as oil spill detections.

Future research work might concern the analysis of the new technique on other available real radar datasets such as AgriSar data [30], as well as its integration in more complex algorithms to produce land cover classifications. Moreover, another possible future work, very suitable for spaceborne applications, might concern the introduction of a fifth hypothesis (H_5), accounting for the presence of acquisition noise only. In this case, if the algorithm decides for H_5 no further processing is possible since no real information on the scene is available.

ACKNOWLEDGMENT

The authors would like to thank the Editor and the Referees for the interesting questions and comments that have helped to improve this article.

This work has been carried out thanks to the financial support of the Italian Ministry of Education, University and Research (MIUR) within the framework of project PON03PE_00159_6 “MoDiSTA - Soluzioni innovative per il Monitoraggio e la Diagnostica preventiva di infrastrutture e flotte di veicoli da remoto al fine di elevare i livelli di disponibilità, efficienza e sicurezza dei siSTemi ferroviAri” and the Engineering and Physical Sciences Research Council (EPSRC) Grant number EP/K014307/1 and the MOD University Defence Research Collaboration in Signal Processing. The authors would also like to acknowledge NASA/JPL for providing the UAVSAR data and ESA for the AIRSAR data.

APPENDIX

A. Proof of Proposition 3.2

We show how the minimization problem (11) can be recast in the presence of the considered symmetry properties, exploiting the results given by Lemma 3.1. Specifically, in the case of reflection symmetry, the minimization problem (11) can be simplified as follows

$$\begin{aligned}
&\min_{\boldsymbol{C}\in\mathcal{H}_3^{++}} \left[\log\det(\boldsymbol{C}) + \text{tr}\left(\boldsymbol{C}^{-1}\boldsymbol{S}\right)\right] \\
&\quad= \min_{\boldsymbol{C}_1\in\mathcal{H}_2^{++}} \left[\log\det(\boldsymbol{C}_1) + \text{tr}\left(\boldsymbol{C}_1^{-1}\bar{\boldsymbol{S}}_{1,1}\right)\right] \\
&\quad+ \min_{c>0}\left[\log(c) + \frac{\bar{S}_{3,3}}{c}\right] \\
&\quad= \log\det\left(\bar{\boldsymbol{S}}_{1,1}\right) + \log\left(\bar{S}_{3,3}\right) + 3,
\end{aligned} \tag{23}$$

Moreover, for the case of rotation symmetry, the objective function reduces to

$$\begin{aligned}
&\log\det(\boldsymbol{C}) + \text{tr}\left(\boldsymbol{C}^{-1}\boldsymbol{S}\right) \\
&\quad= \log\det\left(\boldsymbol{VETCT}^{\dagger}\boldsymbol{EV}^{\dagger}\right) - 2\log\det(\boldsymbol{E}) \\
&\quad+ \text{tr}\left\{\left(\boldsymbol{VETCT}^{\dagger}\boldsymbol{EV}^{\dagger}\right)^{-1}\left(\boldsymbol{VETST}^{\dagger}\boldsymbol{EV}^{\dagger}\right)\right\} \\
&\quad= \log\det(\boldsymbol{C}_2) + \log(a) - 2\log\det(\boldsymbol{E}) \\
&\quad+ \text{tr}\left(\boldsymbol{C}_2^{-1}\tilde{\boldsymbol{S}}_2\right) + \frac{\tilde{S}_{1,1}}{a} \\
&\quad= \log\det(\boldsymbol{C}_2) + \log(a) + \log(2) + \text{tr}\left(\boldsymbol{C}_2^{-1}\tilde{\boldsymbol{S}}_2\right) + \frac{\tilde{S}_{1,1}}{a}.
\end{aligned}$$

Consequently, the minimization problem (11) can be expressed as follows

$$
\begin{aligned}
&\min_{\boldsymbol{C}\in\mathcal{H}_3^{++}} \left[\log\det(\boldsymbol{C}) + \text{tr}\left(\boldsymbol{C}^{-1}\boldsymbol{S}\right)\right] \\
&= \min_{\boldsymbol{C}_2\in\mathcal{S}_2^{++}\cap\mathcal{P}_2^{++}} \left[\log\det(\boldsymbol{C}_2) + \text{tr}\left(\boldsymbol{C}_2^{-1}\tilde{\boldsymbol{S}}_{2,2}\right)\right] \\
&+ \log(\tilde{S}_{1,1}) + 1 + \log(2) \\
&= \min_{\boldsymbol{C}_2\in\mathcal{S}_2^{++}\cap\mathcal{P}_2^{++}} \left[\log\det(\boldsymbol{C}_2)\right. \\
&\left. + \text{tr}\left(\frac{\boldsymbol{C}_2^{-1}}{2}\left(\tilde{\boldsymbol{S}}_{2,2} + \boldsymbol{J}\tilde{\boldsymbol{S}}_{2,2}\boldsymbol{J}\right)\right)\right] \\
&+ \log(\tilde{S}_{1,1}) + 1 + \log(2) \\
&= \log\det\left[\frac{1}{2}\left(\tilde{\boldsymbol{S}}_{2,2} + \boldsymbol{J}\tilde{\boldsymbol{S}}_{2,2}\boldsymbol{J}\right)\right] \\
&+ \log(\tilde{S}_{1,1}) + 3 + \log(2),
\end{aligned} \tag{24}
$$

where in the second equality the persymmetric and real symmetric structure of $\boldsymbol{C}_2$ is used to claim

$$
\text{tr}\left(\boldsymbol{C}_2^{-1}\tilde{\boldsymbol{S}}_{2,2}\right) = \text{tr}\left(\boldsymbol{C}_2^{-1}\boldsymbol{J}\tilde{\boldsymbol{S}}_{2,2}\boldsymbol{J}\right),
$$

and, hence

$$
\text{tr}\left(\boldsymbol{C}_2^{-1}\tilde{\boldsymbol{S}}_{2,2}\right) = \text{tr}\left(\boldsymbol{C}_2^{-1}\frac{1}{2}\left(\tilde{\boldsymbol{S}}_{2,2} + \boldsymbol{J}\tilde{\boldsymbol{S}}_{2,2}\boldsymbol{J}\right)\right). \tag{25}
$$

Finally, for the case of azimuth symmetry, the following equalities hold

$$
\begin{aligned}
&\log\det(\boldsymbol{C}) + \text{tr}\left(\boldsymbol{C}^{-1}\boldsymbol{S}\right) \\
&= \log\det\left(\boldsymbol{E}\boldsymbol{T}\boldsymbol{C}\boldsymbol{T}^\dagger\boldsymbol{E}\right) - 2\log\det(\boldsymbol{E}) \\
&+ \text{tr}\left\{\left(\boldsymbol{E}\boldsymbol{T}\boldsymbol{C}\boldsymbol{T}^\dagger\boldsymbol{E}\right)^{-1}\left(\boldsymbol{E}\boldsymbol{T}\boldsymbol{S}\boldsymbol{T}^\dagger\boldsymbol{E}\right)\right\} \\
&= \log(a) + 2\log(b) + \log(2) + \frac{\hat{S}_{1,1}}{a} \\
&+ \frac{\hat{S}_{2,2} + \hat{S}_{3,3}}{b},
\end{aligned} \tag{26}
$$

and the minimization problem (11) can be rewritten as

$$
\begin{aligned}
&\min_{\boldsymbol{C}\in\mathcal{H}_3^{++}} \left[\log\det(\boldsymbol{C}) + \text{tr}\left(\boldsymbol{C}^{-1}\boldsymbol{S}\right)\right] \\
&= \log(\hat{S}_{1,1}) + 2\log\left(\frac{\hat{S}_{2,2} + \hat{S}_{3,3}}{2}\right) + 3 + \log(2).
\end{aligned} \tag{27}
$$

B. Computation of $\boldsymbol{F}$ and Regularity Conditions

We verify, for the BIC rule, the regularity conditions that must hold on the Fisher information matrix $\boldsymbol{F}$:

1) Invertibility of the Fisher Information Matrix: The ML estimator of the parameter vector (synthetically denoted by $\hat{\boldsymbol{\theta}}$) is unbiased and with finite variance. Hence by [31, Equation (18)], applied with $\boldsymbol{H} = \boldsymbol{I}$,

$$
\boldsymbol{I} = \boldsymbol{F}\boldsymbol{F}^+,
$$

must hold. This is true if and only if $\boldsymbol{F}$ is invertible.

2) Regularity Condition: $\frac{\boldsymbol{F}}{K} = O(1)$: By Slepian-Bangs formula of [32, p. 927],

$$
F_{i,j} = K \ \text{tr}\left[\boldsymbol{C}^{-1}(\hat{\boldsymbol{\theta}})\frac{\partial\boldsymbol{C}(\boldsymbol{\theta})}{\partial\theta_i}\boldsymbol{C}^{-1}(\hat{\boldsymbol{\theta}})\frac{\partial\boldsymbol{C}(\boldsymbol{\theta})}{\partial\theta_j}\right]. \tag{28}
$$

Since, $\boldsymbol{C}(\hat{\theta})$ tends to the true covariance as $K \to \infty$, whereas the terms $A_i = \partial\boldsymbol{C}(\boldsymbol{\theta})/\partial\theta_i$ and $A_j = \partial\boldsymbol{C}(\boldsymbol{\theta})/\partial\theta_j$ do not depend on K

$$
\frac{F_{i,j}}{K} \to \text{tr}\left[\boldsymbol{C}(\boldsymbol{\theta})^{-1}A_i\boldsymbol{C}(\boldsymbol{\theta})^{-1}A_j\right] = O(1). \tag{29}
$$

REFERENCES

[1] J. S. Lee and E. Pottier, *Polarimetric Radar Imaging: From Basics to Applications*, CRC Press, 2009.

[2] S. V. Nghiem, S. H. Yueh, R. Kwok, and F. K. Li, "Symmetry Properties in Polarimetric Remote Sensing," *Radio Science*, vol. 27, no. 5, pp. 693–711, September-October 1992.

[3] L. Ferro-Famil and E. Pottier (Editor in Chief J. A. Kong), *Progress In Electromagnetics Research*, vol. 24, chapter Dual Frequency Polarimetric SAR Data Classification and Analysis, pp. 251–276, New York Elsevier, 2001.

[4] J. C. Curlander and R. N. McDonough, *Synthetic Aperture Radar*, John Wiley & Sons, 1991.

[5] S. R. Cloude and E. Pottier, "A Review of Target Decomposition Theorems in Radar Polarimetry," *IEEE Trans. on Geoscience and Remote Sensing*, vol. 34, no. 2, pp. 498–518, March 1996.

[6] E. Krogager, "New Decomposition of the Radar Target Scattering Matrix," *Electronics Letters*, vol. 26, no. 18, pp. 1525–1527, 1990.

[7] W. L. Cameron and L. K. Leung, "Feature Motivated Polarization Scattering Matrix Decomposition," in *IEEE International Radar Conference*, Arlington, VA, May 7-10 1990.

[8] S. R. Cloude and E. Pottier, "An Entropy Based Classification Scheme for Land Applications of Polarimetric SAR," *IEEE Trans. on Geoscience and Remote Sensing*, vol. 35, no. 1, pp. 68–78, January 1997.

[9] J. J. Van Zyl, "Unsupervised Classification of Scattering Behavior Using Radar Polarimetry Data," *IEEE Trans. on Geoscience and Remote Sensing*, vol. 27, no. 1, pp. 36–45, January 1989.

[10] S. E. Park, W. M. Moon, and E. Pottier, "Assessment of Scattering Mechanism of Polarimetric SAR Signal From Mountainous Forest Areas," *IEEE Trans. on Geoscience and Remote Sensing*, vol. 50, no. 11, pp. 4711–4719, 2012.

[11] M. Migliaccio, F. Nunziata, A. Montuori, L. Xiaofeng, and W. G. Pichel, "A Multifrequency Polarimetric SAR Processing Chain to Observe Oil Fields in the Gulf of Mexico," *IEEE Trans. on Geoscience and Remote Sensing*, vol. 49, no. 12, pp. 4729–4737, December 2011.

[12] A. B. Salberg, O. Rudjord, and A. H. S. Solberg, "Oil Spill Detection in Hybrid-Polarimetric SAR Images," *IEEE Trans. on Geoscience and Remote Sensing*, vol. 52, no. 10, pp. 6521–6533, Oct 2014.

[13] S. Mermoz, S. Allain-Bailhache, M. Bernier, E. Pottier, J. J. van der Sanden, and K. Chokmani, "Retrieval of River Ice Thickness From C-Band PolSAR Data," *IEEE Trans. on Geoscience and Remote Sensing*, vol. 52, no. 6, pp. 3052–3062, June 2014.

[14] G. Zhou, Y. Cui, Y. Chen, J. Yang, H. Rashvand, and Y. Yamaguchi, "Linear Feature Detection in Polarimetric SAR Images," *IEEE Trans. on Geoscience and Remote Sensing*, vol. 49, no. 4, pp. 1453–1463, April 2011.

[15] S. M. Kay, *Fundamentals of Statistical Signal Processing: Estimation Theory*, vol. 1, Prentice Hall, 1993.

[16] S. M. Kay, "The Multifamily Likelihood Ratio Test for Multiple Signal Model Detection," *IEEE Signal Processing Letters*, vol. 12, no. 5, pp. 369–371, May 2005.

[17] Y. Selén, *Model Selection*, Phd dissertation in electrical engineering, Uppsala University, Sweden, October 2004.

[18] P. Stoica and Y. Selén, "Model-Order Selection: A Review of Information Criterion Rules," *IEEE Signal Processing Magazine*, vol. 21, no. 4, pp. 36–47, 2004.

[19] P. Stoica, Y. Selén, and J. Li, "On Information Criteria and the Generalized Likelihood Ratio Test of Model Order Selection," *IEEE Signal Processing Letters*, vol. 11, no. 10, pp. 794–797, 2004.

[20] S. M. Kay, "Exponentially Embedded Families-New Approaches to Model Order Estimation," *IEEE Trans. on Aerospace and Electronic Systems*, vol. 41, no. 1, pp. 333–345, January 2005.

[21] F. Bordoni, F. Gini, and L. Verrazzani, "Capon-LS for Model Order Selection of Multicomponent Interferometric SAR Signals," in *IEE Proceedings Radar, Sonar and Navigation*, 2004, vol. 151, pp. 299–305.

[22] F. Lombardini, L. Rößing, J. Ender, and F. Cai, "Interferometric Model Order Selection: Validation of ITC Methods with Airborne Three-Antenna SAR Data," in *IEEE International Conference on Geoscience and Remote Sensing Symposium (IGARSS)*, 2006, pp. 2565–2568.

[23] S. Sauer, L. Ferro-Famil, A. Reigber, and E. Pottier, "Physical Parameter Extraction Over Urban Areas Using L-band POLSAR Data and Interferometric Baseline Diversity," in *IEEE International Conference on Geoscience and Remote Sensing Symposium (IGARSS)*, 2007, pp. 5045–5048.

[24] F. Lombardini and F. Gini, "Model Order Selection in Multi-Baseline Interferometric Radar Systems," *EURASIP Journal on Applied Signal Processing*, vol. 20, no. 20, pp. 3206–3219, 2005.

[25] A. Pauciullo, D. Reale, A. De Maio, and G. Fornaro, "Detection of Double Scatterers in SAR Tomography," *IEEE Trans. on Geoscience and Remote Sensing*, vol. 50, no. 9, pp. 3567–3586, 2012.

[26] E. Conte and M. Longo, "Characterisation of Radar Clutter as a Spherically Invariant Random Process," *IEE Proceedings Communications, Radar and Signal Processing*, vol. 134, no. 2, pp. 191–197, April 1987.

[27] M. Greco and F. Gini, "Statistical Analysis of High-Resolution SAR Ground Clutter Data," *IEEE Trans. on Geoscience and Remote Sensing*, vol. 45, no. 3, pp. 566–575, March 2007.

[28] C. Oliver and S. Quegan, *Understanding Synthetic Aperture Radar Images*, SciTech Publishing, 2004.

[29] S. Hensley et al., "The UAVSAR Instrument: Description and First Results," in *IEEE International Radar Conference*, May 2008, pp. 1–6.

[30] G. Di Martino, A. Iodice, A. Natale, and D. Riccio, "Polarimetric Two-Scale Two-Component Model for the Retrieval of Soil Moisture Under Moderate Vegetation via L-Band SAR Data," *IEEE Trans. on Geoscience and Remote Sensing*, vol. 54, no. 4, pp. 2470–2491, 2016.

[31] P. Stoica and T. L. Marzetta, "Parameter Estimation Problems with Singular Information Matrices," *IEEE Trans. on Signal Processing*, vol. 49, no. 1, pp. 87–90, January 2001.

[32] H. L. Van Trees, *Detection, Estimation and Modulation Theory: Optimum Array Processing*, John Wiley & Sons, 2002.

Luca Pallotta (S'12, M'15) received the Laurea Specialistica degree (cum laude) in telecommunication engineering in 2009 from the University of Sannio, Benevento, Italy, and the Ph.D. degree in electronic and telecommunication engineering in 2014 from the University of Naples Federico II, Naples, Italy. His research interest lies in the field of statistical signal processing, with emphasis on radar signal processing, radar targets classification, SAR images classification. Dr. Pallotta won the Student Paper Competition at the IEEE Radar Conference 2013.

Carmine Clemente (S'09-M'13) received the Laurea cum laude (BSc) and Laurea Specialistica cum laude (MSc) degrees in telecommunications engineering from Universita' degli Studi del Sannio, Benevento, Italy, in 2006 and 2009, respectively. In 2012, he received the Ph.D. degree in the Department of Electronic and Electrical Engineering, University of Strathclyde, Glasgow, UK. Currently he is a Lecturer in the Department of Electronic and Electrical Engineering, University of Strathclyde, Glasgow, U.K working on advanced Radar signal processing algorithm, MIMO radar systems and micro-Doppler analysis. His research interests include synthetic aperture radar (SAR) focusing and bistatic SAR focusing algorithms development, micro-Doppler signature analysis and extraction from multistatic radar platforms, micro-Doppler classification and statistical signal processing.

Antonio De Maio (S'01-A'02-M'03-SM'07-F'13) was born in Sorrento, Italy, on June 20, 1974. He received the Dr.Eng. degree (with honors) and the Ph.D. degree in information engineering, both from the University of Naples Federico II, Naples, Italy, in 1998 and 2002, respectively. From October to December 2004, he was a Visiting Researcher with the U.S. Air Force Research Laboratory, Rome, NY. From November to December 2007, he was a Visiting Researcher with the Chinese University of Hong Kong, Hong Kong. Currently, he is a Professor with the University of Naples Federico II. His research interest lies in the field of statistical signal processing, with emphasis on radar detection, optimization theory applied to radar signal processing, and multiple-access communications. Dr. De Maio is the recipient of the 2010 IEEE Fred Nathanson Memorial Award as the young (less than 40 years of age) AESS Radar Engineer 2010 whose performance is particularly noteworthy as evidenced by contributions to the radar art over a period of several years, with the following citation for "robust CFAR detection, knowledge-based radar signal processing, and waveform design and diversity". Dr. De Maio also is a Fellow member of IEEE.

John J. Soraghan (S'83-M'84-SM'96) received the B.Eng. (Hons.) and M.Eng.Sc. degrees in electronic engineering from University College Dublin, Dublin, Ireland, in 1978 and 1983, respectively, and the Ph.D. degree in electronic engineering from the University of Southampton, U.K., in 1989. His doctoral research focused on synthetic aperture radar processing on the distributed array processor. After graduating, he worked with the Electricity Supply Board in Ireland and with Westinghouse Electric Corporation in the United States. In 1986, he joined the Department of Electronic and Electrical Engineering, University of Strathclyde, Glasgow, U.K., as a Lecturer and became a Senior Lecturer in 1990, a Reader in 2000, and a Professor in Signal Processing in September 2003, within the Institute for Communications and Signal Processing (ICSP). In December 2005, he became the Head of the ICSP. He currently holds the Texas Instruments Chair in Signal Processing with the University of Strathclyde. He was a Manager of the Scottish Transputer Centre from 1988 to 1991, and a Manager of the DTI Parallel Signal Processing Centre from 1991 to 1995. His main research interests are signal processing theories, algorithms and architectures with applications to remote sensing, telecommunications, biomedicine, and condition monitoring. Prof. Soraghan is a member of the IET and IEEE.

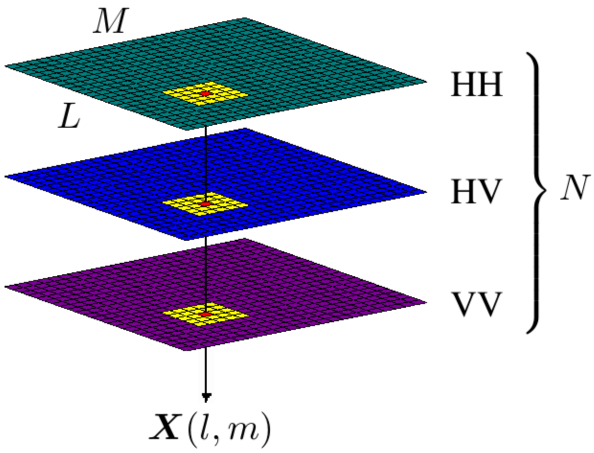

Fig. 1: A pictorial representation to construct the datacube for polarimetric images.

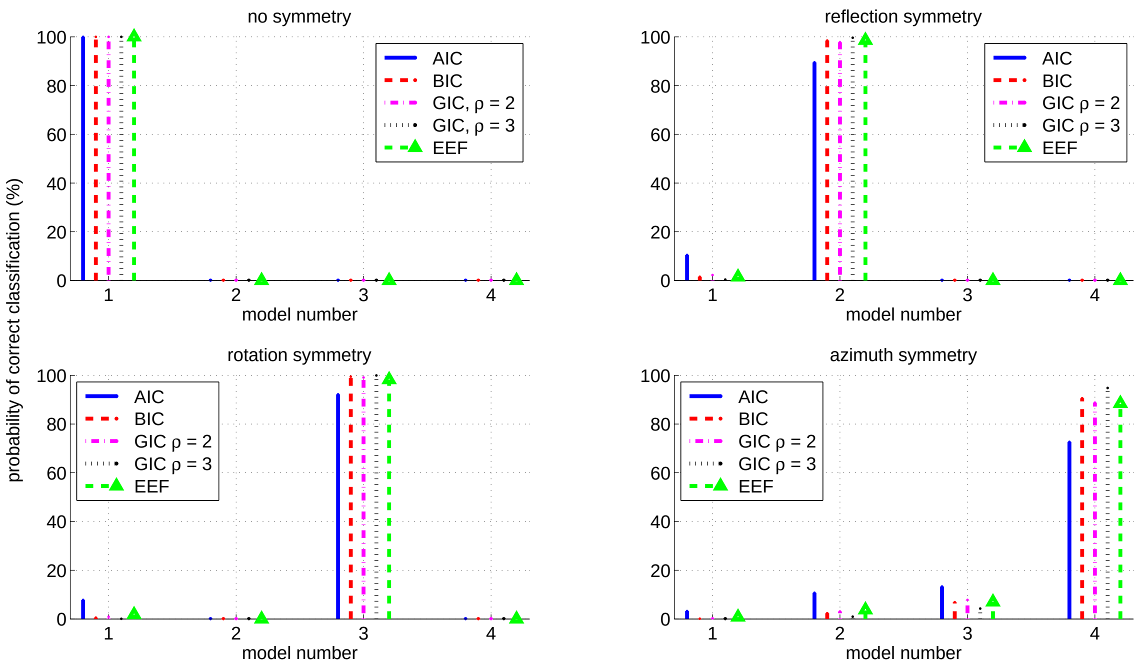

Fig. 2: Probability of correct classification $(\%)$ for a simulated scenario with $K = 25$ data and $MC = 10^4$ Monte Carlo trials.

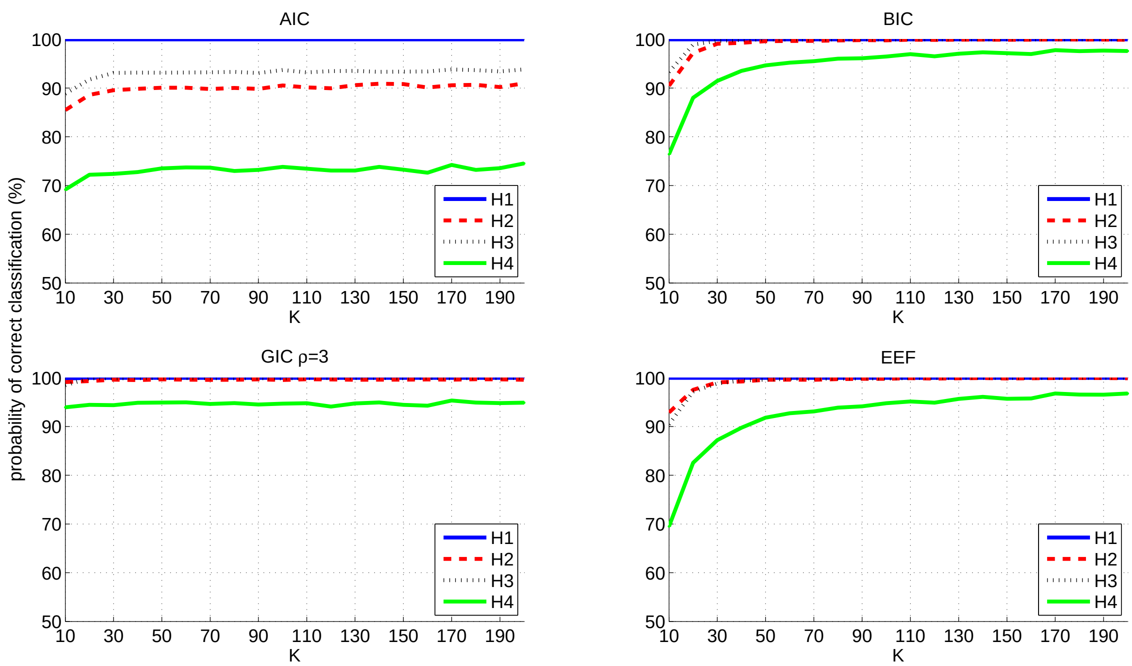

Fig. 3: Probability of correct classification $(\%)$ versus the number of data K, with $MC = 10^4$ Monte Carlo trials. The subplots refer to the different selectors, whereas the curves are related to the four considered covariance scenarios, i.e. $\boldsymbol{C}_1$, $\boldsymbol{C}_2$, $\boldsymbol{C}_3$, and $\boldsymbol{C}_4$.

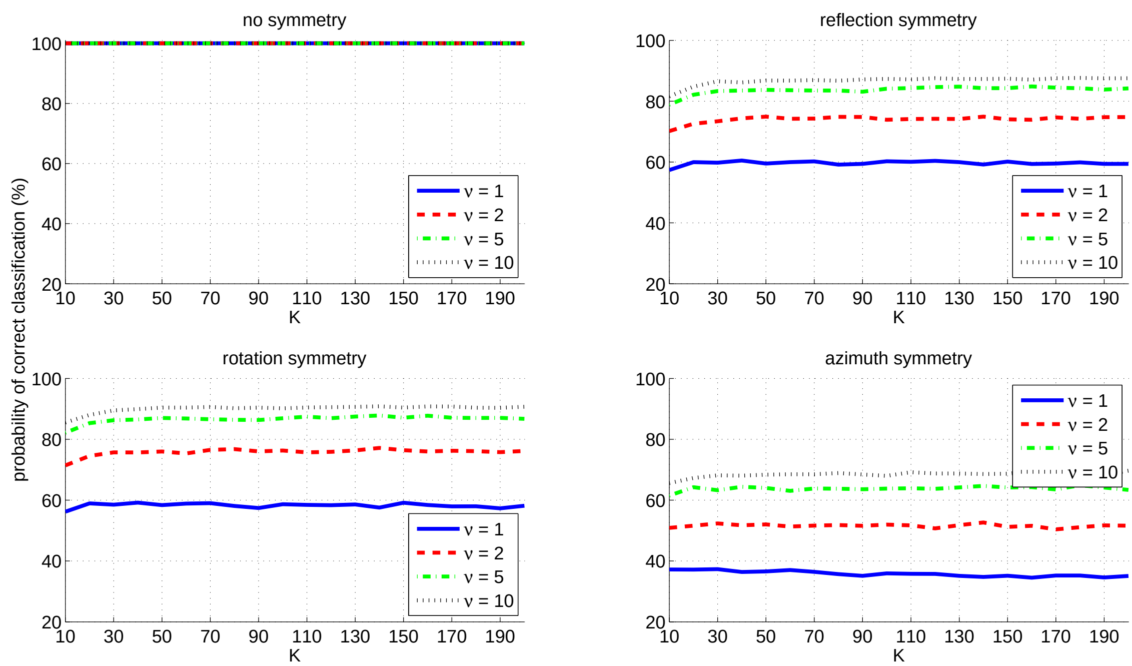

Fig. 4: Probability of correct classification $(\%)$ for the AIC selector versus the number of data K in a SIRV environment, with $MC = 10^4$ Monte Carlo trials. The subplots refer to the different covariance scenarios, i.e. $\boldsymbol{C}_1$, $\boldsymbol{C}_2$, $\boldsymbol{C}_3$, and $\boldsymbol{C}_4$, whereas the curves refer to the four considered values of ν.

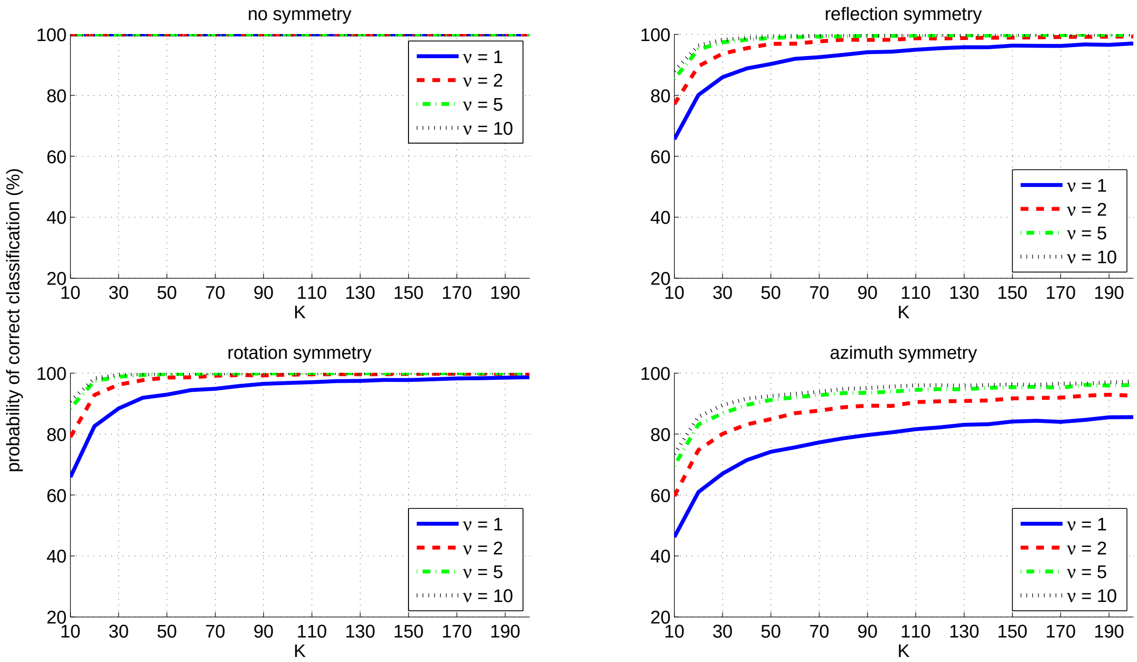

Fig. 5: Probability of correct classification (%) for the BIC selector versus the number of data K in a SIRV environment, with $MC = 10^4$ Monte Carlo trials. The subplots refer to the different covariance scenarios, i.e. $\boldsymbol{C}_1$, $\boldsymbol{C}_2$, $\boldsymbol{C}_3$, and $\boldsymbol{C}_4$, whereas the curves refer to the four considered values of ν.

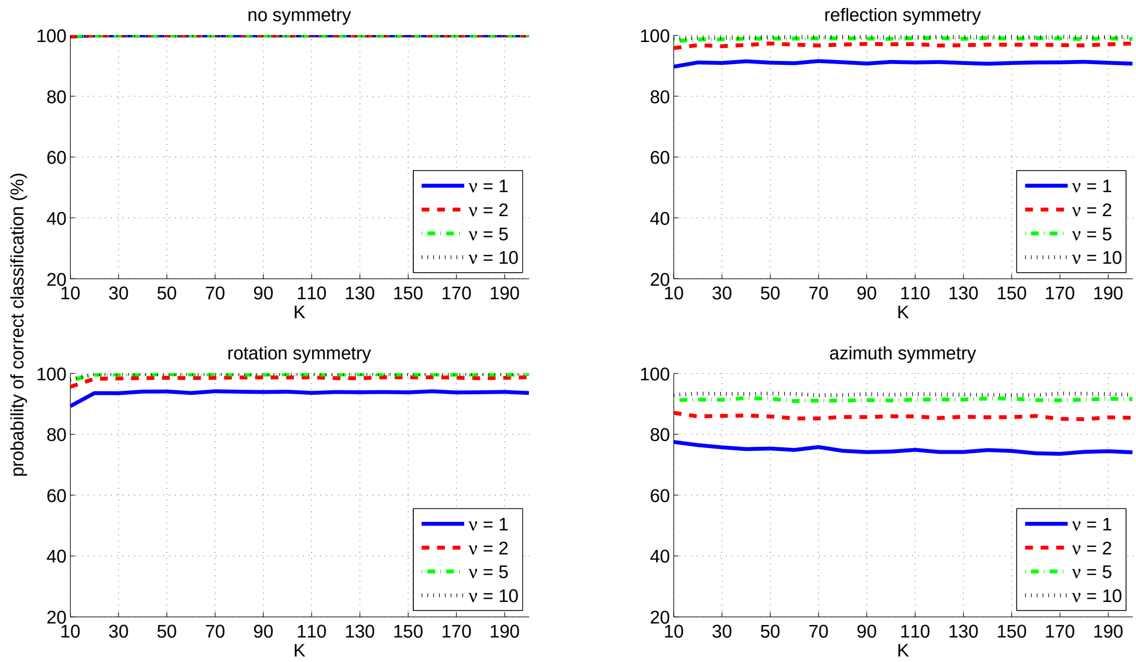

Fig. 6: Probability of correct classification (%) for the GIC (with $\rho = 3$) selector versus the number of data K in a SIRV environment, with $MC = 10^4$ Monte Carlo trials. The subplots refer to the different covariance scenarios, i.e. $\boldsymbol{C}_1$, $\boldsymbol{C}_2$, $\boldsymbol{C}_3$, and $\boldsymbol{C}_4$, whereas the curves refer to the four considered values of ν.

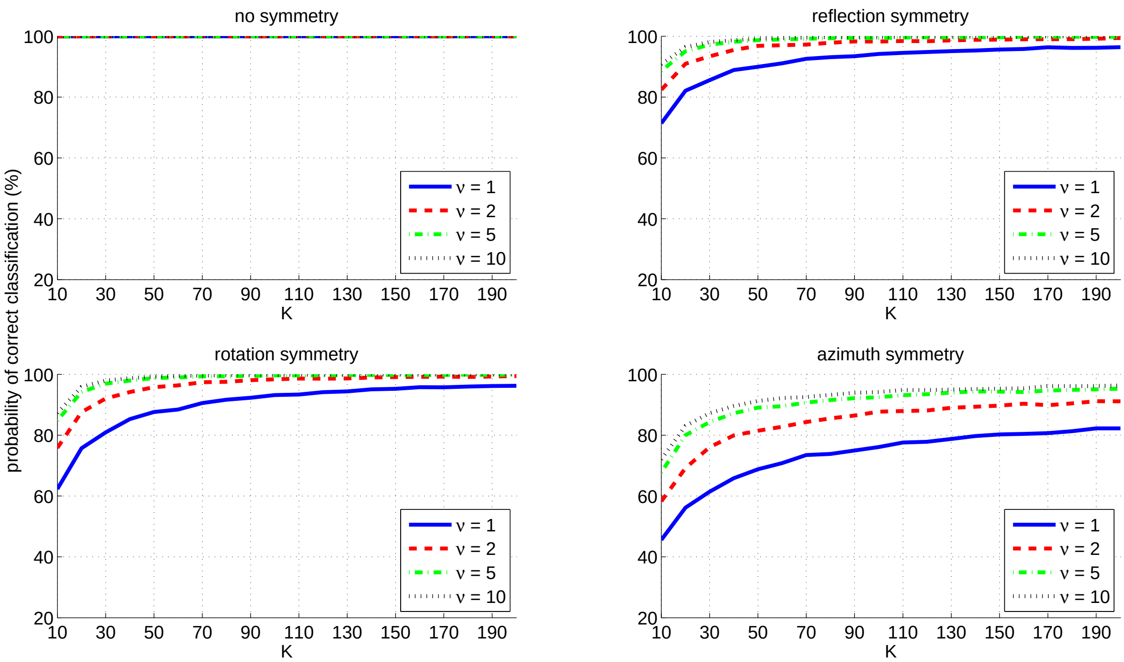

Fig. 7: Probability of correct classification (%) for the EEF selector versus the number of data K in a SIRV environment, with $MC = 10^4$ Monte Carlo trials. The subplots refer to the different covariance scenarios, i.e. $\boldsymbol{C}_1$, $\boldsymbol{C}_2$, $\boldsymbol{C}_3$, and $\boldsymbol{C}_4$, whereas the curves refer to the four considered values of ν.

Fig. 8: Three polarization color overlay of the UAVSAR pass SSurge_15305_14170_007_141120_L090_CX_01.

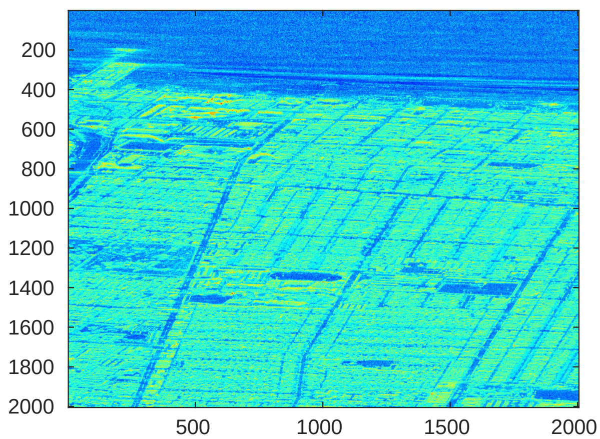

(a) span

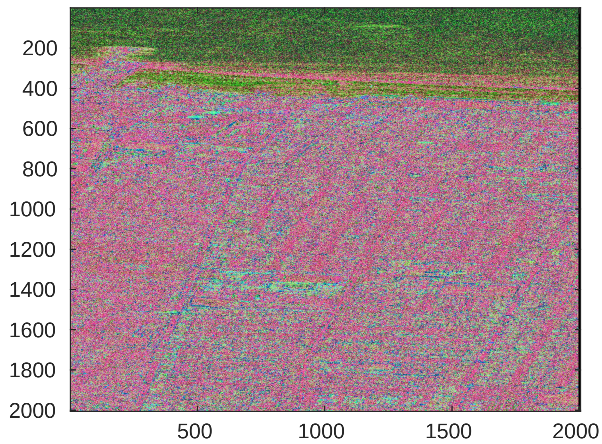

(b) H-A-α decomposition

Fig. 9: Real L-band data UAVSAR pass SSurge_15305_14170_007_141120_L090_CX_01. (a) Span (b) RGB of the H-A-α decomposition for the reference image of size 2000×2000 pixels.

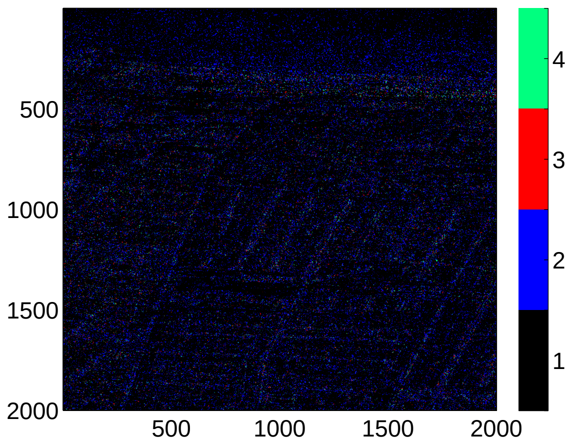

(a) AIC

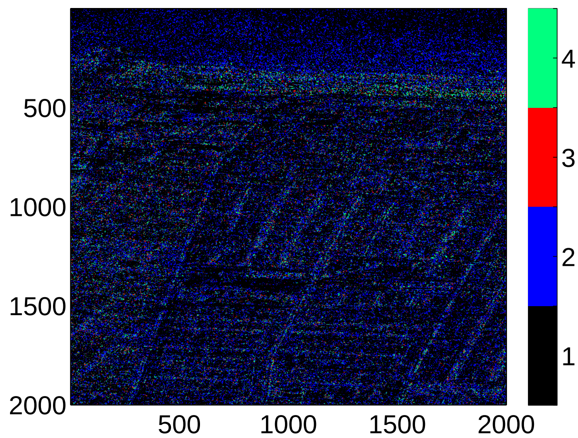

(b) BIC

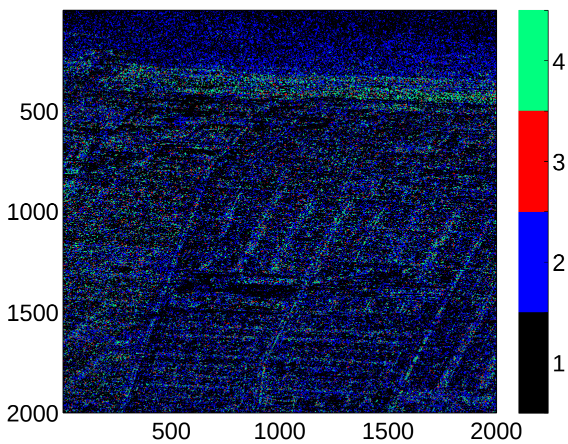

(c) GIC, $\rho = 3$

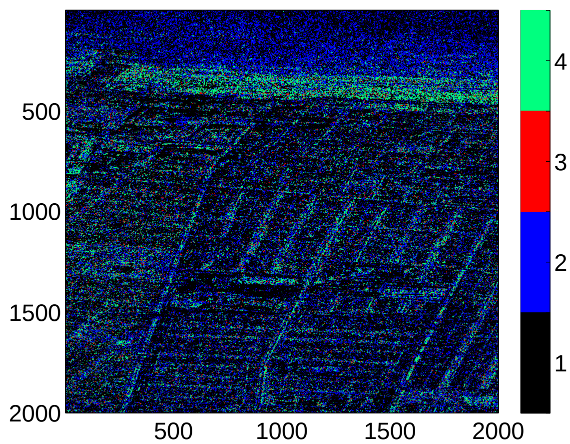

(d) EEF

Fig. 10: Real L-band data UAVSAR pass SSurge_15305_14170_007_141120_L090_CX_01. Detected symmetries within the reference image, $K = 25$.

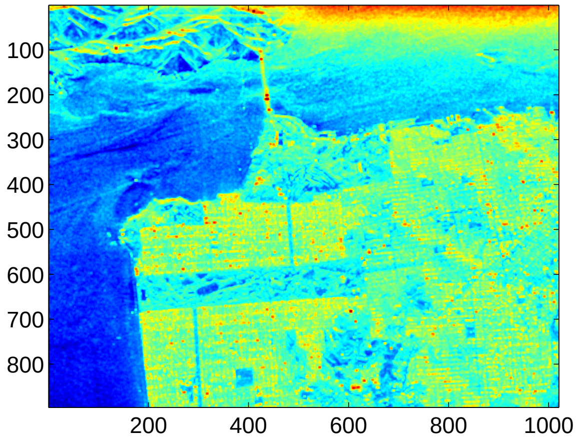

(a) span

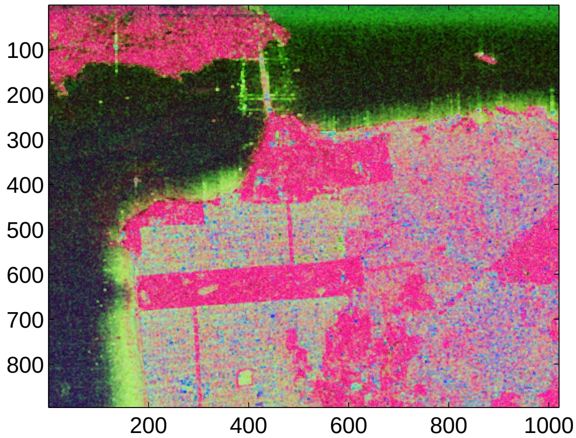

(b) H-A-α decomposition

Fig. 11: San Francisco Bay JPL (AIRSAR L-band 1988) data. (a) Span (in dB) (b) RGB of the H-A-α decomposition for the reference image of size 900×1024 pixels.

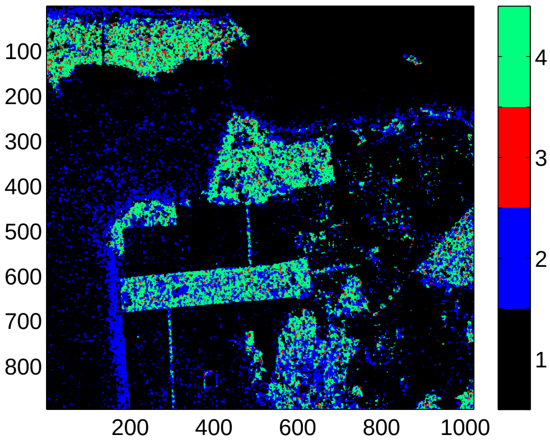

(a) AIC

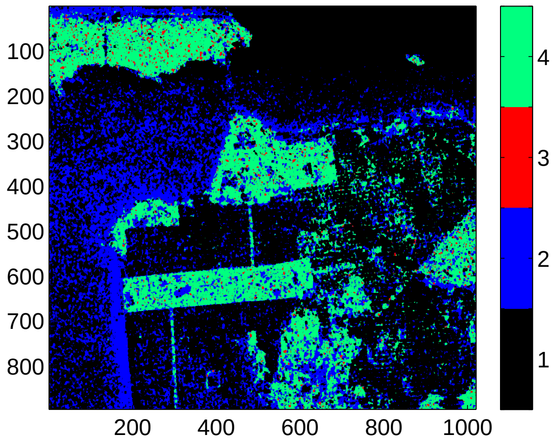

(b) BIC

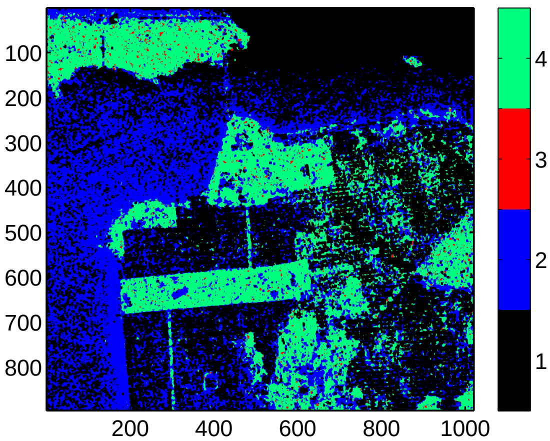

(c) GIC, $\rho = 3$

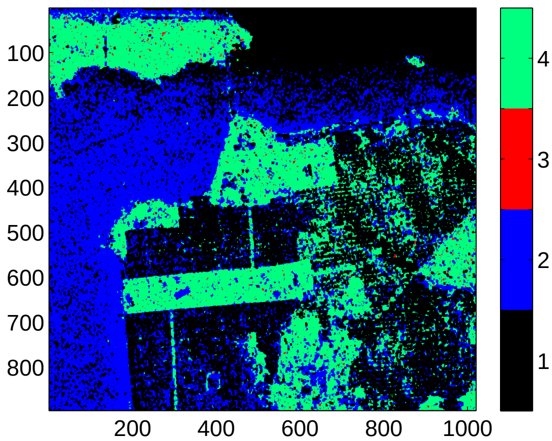

(d) EEF

Fig. 12: Real L-band data AIRSAR San Francisco Bay JPL. Detected symmetries within the reference image, $K = 25$.

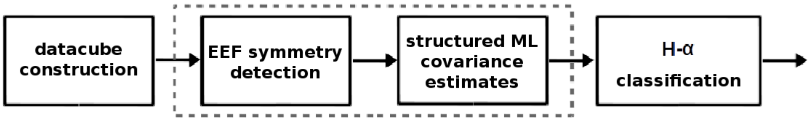

Fig. 13: Block scheme of the symmetric H-α classification.

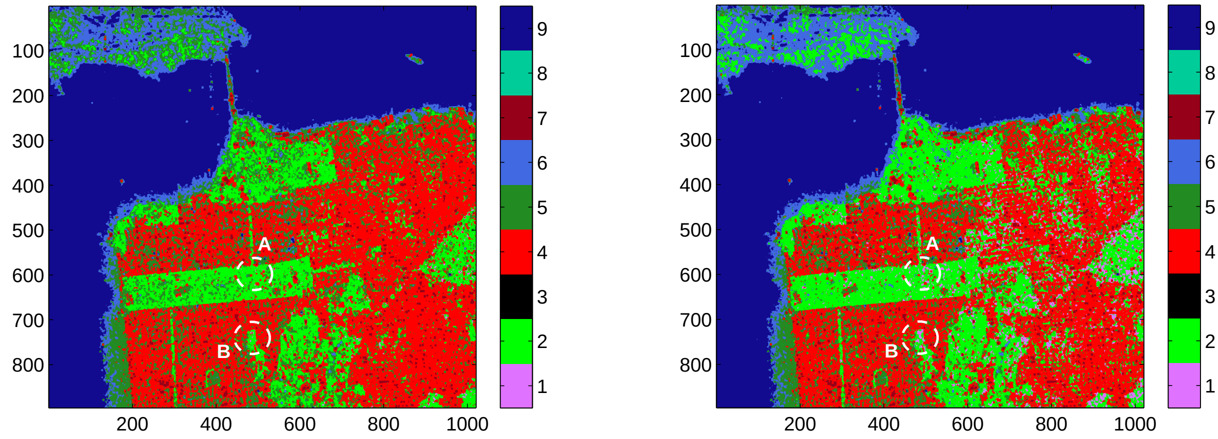

(a) H-α classifier

(b) Symmetric H-α classifier

Fig. 14: Real L-band data (AIRSAR San Francisco Bay JPL). H-α classification.

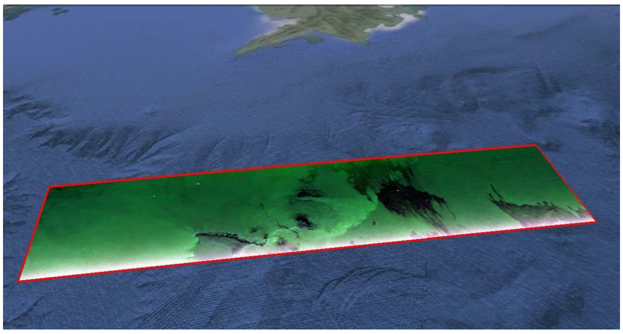

Fig. 15: Three polarization color overlay of the SAR image GOMoil_07601_10052_101_100622_L090_CX_02.

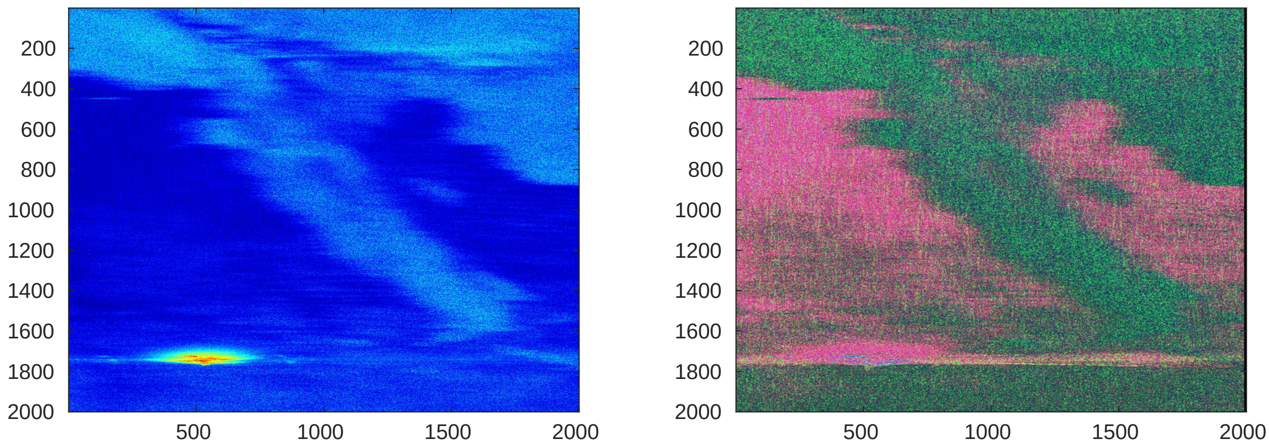

(a) span

(b) H-A-α decomposition

Fig. 16: Real L-band data SAR image GOMoil_07601_10052_101_100622_L090_CX_02. (a) Span (in dB) (b) RGB of the H-A-α decomposition for the reference image of size 2000×2000 pixels.

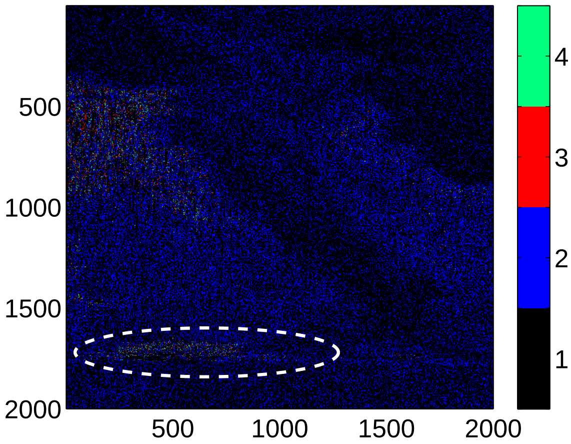

(a) AIC

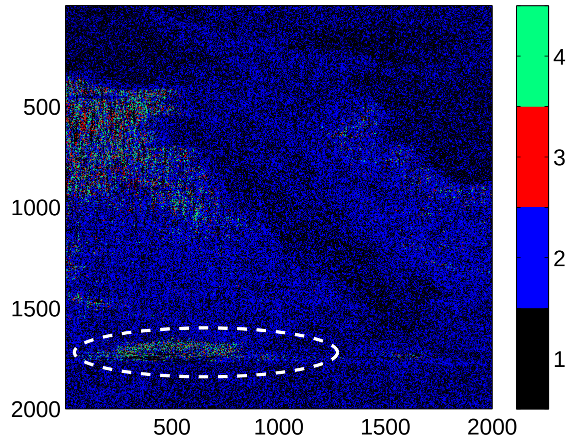

(b) BIC

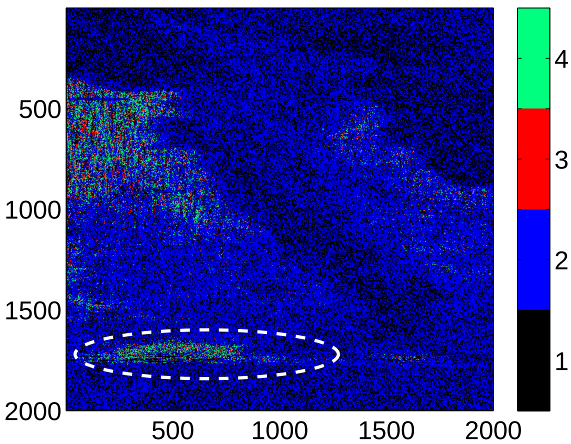

(c) GIC, $\rho = 3$

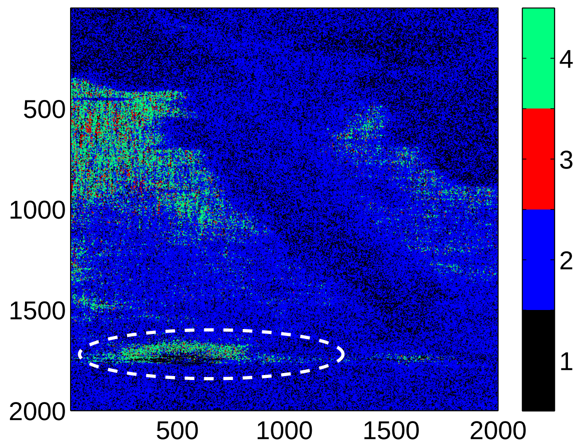

(d) EEF

Fig. 17: Real L-band data SAR image GOMoil_07601_10052_101_100622_L090_CX_02. Detected symmetries within the reference image, $K = 25$.